

Identification of Dominant Features in Spatial Data

Roman Flury^a, Florian Gerber^c, Bernhard Schmid^d, Reinhard Furrer^{a,b}

^a*Department of Mathematics, University of Zurich, Zurich, Switzerland*

^b*Department of Computational Science, University of Zurich, Zurich, Switzerland*

^c*Department of Applied Mathematics and Statistics, Colorado School of Mines, Golden, USA*

^d*Department of Geography, University of Zurich, Zurich, Switzerland*

Abstract

Dominant features of spatial data are structures or patterns that become manifest at specific scales or resolutions. To identify dominant features, we propose a sequential application of multiresolution decomposition and variogram function estimation. Multiresolution decomposition separates data into additive components, and in this way enables the recognition of their dominant features. A dedicated multiresolution decomposition method is developed for arbitrary gridded spatial data, where the underlying model includes a precision and spatial-weight matrix to capture spatial correlation. The data are separated into their components by smoothing on different scales, such that larger scales have longer spatial correlation ranges. Moreover, our model can handle missing values, which is often useful in applications. Properties in spatial data can be described with variogram functions. These are therefore estimated for each component to determine its effective-range, which assesses the width-extent of the dominant feature. Finally, Bayesian analysis enables the inference of identified dominant features and to judge whether these are credibly different. The efficient implementation of the method relies mainly on a sparse-matrix data structure and algorithms. By applying the method to simulated data we demonstrate its applicability and theoretical soundness. In disciplines that use spatial data, this method can lead to new insights, as we exemplify by identifying the dominant features in a forest dataset. In that application, the width-extents of the dominant features have an ecological interpretation, namely the species interaction range, and their estimates support the derivation of ecosystem properties such as biodiversity indices.

Keywords: Scale-space analysis, Lattice data, Gaussian Markov random field, Moving-window size.

1. Introduction

In various scientific disciplines, including ecology, epidemiology, climate science, hydrology, and fluid dynamics, relevant questions are often associated with specific scale-dependent features of the data. In this context, a scale describes the approximate resolution or geographic extent in which a phenomenon or feature becomes manifest. Typically one expects to identify noise or micro, local, regional or global scales in the data (Wikle and Berliner, 2005; Wu, 2013). The detection of all relevant scales and the identification of their dominant features are essential for a complete statistical analysis. Assuming that every scale is characterized by dominant features, the assessment of the *feature width-extent* is of equal importance. These widths help to understand the scale-dependent features themselves and their relation to underlying mechanisms (Delcourt and Delcourt, 1988; Skøien et al., 2003; Pasanen et al., 2018).

To find relevant scales in spatial data, existing signal-decomposition and image-processing methods are applied. Decomposition approaches were first proposed in the computer-vision literature (Witkin, 1983; Lindeberg, 1994) and were subsequently adapted in statistical scale-space analysis, where a sample path is considered at several scales. The scales are then obtained through appropriate smoothing (Chaudhuri and

Email addresses: roman.flury@math.uzh.ch (Roman Flury), reinhard.furrer@math.uzh.ch (Reinhard Furrer)

Marron, 1999). These ideas were extended by Holmström (2010) and are now known as *Bayesian significant zero crossings of derivatives* and *scale-space analysis*. The main goal of scale-space analysis is to recognize scale-dependent features from time-series data and images (Holmström et al., 2011), as was successfully demonstrated in several applied studies (Lehmann et al., 2017; Aakala et al., 2018; Kulha et al., 2019).

Methods to assess *feature width-extents* directly from the data are used in spectral analysis, introduced by Ford and Renshaw (1984) and applied, for instance, in Stoll et al. (1994). However, Pasanen et al. (2018) were the first to describe an approach to determine the actual size of scale-dependent features. They showed that the maximum of the so-called scale-derivative norm (Pasanen et al., 2013) of a recognized component can be used to estimate its *characteristic feature size*.

In spatial statistics, data properties are often described with variogram or covariance functions and their respective parameters. Depending on the dimension of the data, the approximation of their parameters becomes computationally intensive. Therefore, *spatial multiresolution models* have been developed to reduce the resolution in the data while preserving their information content. These models often use a linear combination of basic functions to model spatially dependent data. The coefficients are then usually estimated to weight the respective basis functions (Cressie and Johannesson, 2008; Katzfuss and Cressie, 2012; Nychka et al., 2015), or chosen to approximate a given covariance function optimally (Katzfuss, 2017).

In this article, we first develop a multiresolution decomposition for spatial data on the basis of the statistical scale space method of Holmström et al. (2011) (Section 2). This scale space analysis and its implementation are only applicable to complete and regularly gridded data. However, spatial data typically contains dependencies along any direction and their intensity is usually strongly linked to the distance between locations and becomes weaker as the distance increases (Cressie, 1993). Depending on the spatial environment, it is also possible that there is no dependency between specific locations. Therefore, we propose a decomposition method that enables accurate modeling of the dependency and neighboring relations between locations. The newly developed method is applicable for arbitrary gridded spatial data, where the resolution of the grid points defines the aggregation of the represented area. With this method, it is possible to exclude specific grid locations that are not relevant for the analysis or without assigned value. Accounting for the latter case, we introduce a flexible procedure to resample missing values in the data.

In addition, we propose assessing the width-extents of the dominant scale-dependent features (Section 2.4). To do so, we estimate the empirical variogram (Matheron, 1962; Cressie, 1993) and optimize a Matérn variogram function for its parameters. We assess the width-extent of the individual scale-dependent features with its respective effective-range parameter (Pebesma, 2004; Nychka et al., 2020). Importantly, unlike in multiresolution models, we do not reduce the dimensionality in the data, while preserving their information content to approximate a covariance function efficiently. But by approximating a variogram function based on each component separately, we identify the width-extents of the dominant scale-dependent feature in largest-possible isolation.

We first apply the new method to simulated data (Section 3). In this setting, we can control the parameters of the additive spatial data and demonstrate the consistency of the results. Second, we demonstrate the usefulness of the method by an application (Section 4) in which we explain how the identification of dominant features can be used to find different area sizes in which communities of species interact with each other (Greig-Smith, 1979). The diameter of such a relevant community of species is known as the interaction range. It can be used to determine different radii for multidimensional biodiversity indices based on moving-window approaches. In this application, we use scientifically relevant data, which were obtained by remote sensing from the forest on the hillslope of mountain Laegeren in Switzerland. For this area, multidimensional functional-biodiversity indices were calculated in previous studies and evaluated at different radii determined by experts.

2. Feature identification

2.1. Spatial data resampling based on a Bayesian hierarchical model

As in the scale-space analysis method, we assume that the observed dataset \mathbf{y} is a composition of the true underlying data \mathbf{x} and additional white noise $\boldsymbol{\varepsilon}$ with constant variance. To separate observational noise

from the unobserved data, \mathbf{y} is modeled and resampled using a Bayesian model (Gelfand, 2012). For the inferred features, credibility maps can then be derived to distinguish noise from these features (Erästö and Holmström, 2005). In the scale-space analysis, the Bayesian model is constructed such that its posterior distribution is of closed form and that it is possible to calculate the inverse of the precision matrix by fast Fourier transformation (Strang, 1999; Reuter et al., 2009). However, these computational gains restrict this method to complete and regularly gridded data with a fixed precision matrix. To remove these restrictions on the data and enable arbitrary precision matrices, we need to replace the efficient fast Fourier transformation implementation. As precision matrices are typically sparse, we can rely on its economic data structure and efficient algorithms. For the statistical software R those are implemented, for example, in the **spam** package (Furrer and Sain, 2010). Having the possibility to represent the precision matrix of extensive spatial data, the calculation of its inverse — the covariance matrix — remains computationally expensive (see Section 2.6 for more computational details). For this reason, we choose a normal-gamma model to resample spatial data (Rue and Held, 2005). With this model, it is possible to sample from the canonical representation of a multivariate normal distribution, where the inverse of the precision matrix does not need to be calculated explicitly.

The normal-gamma model includes a multivariate normal likelihood function for the observed dataset \mathbf{y} at conditionally independent locations, with the true mean \mathbf{x} and precision parameter $\kappa_{\mathbf{y}}$. It is proportional to

$$\pi(\mathbf{y}|\mathbf{x}, \kappa_{\mathbf{y}}) \propto \kappa_{\mathbf{y}}^{n/2} \exp\left(-\frac{\kappa_{\mathbf{y}}}{2} (\mathbf{y} - \mathbf{x})^\top (\mathbf{y} - \mathbf{x})\right),$$

where n denotes the total number of locations in the spatial data. To model the spatial dependencies of \mathbf{x} , we use an intrinsic Gaussian Markov Random Field (IGMRF) with zero mean, a precision parameter κ_x , and a spatial-weight matrix \mathbf{Q} , which represents the dependencies between locations.

$$\pi(\mathbf{x}|\kappa_x) \propto \kappa_x^{(n-2)/2} \exp\left(-\frac{\kappa_x}{2} \mathbf{x}^\top \mathbf{Q} \mathbf{x}\right). \quad (1)$$

For the unknown precision parameters of the normal likelihood and the spatial process, we choose independent Gamma distributions, the respective conjugate prior distributions. The according prior distributions have strictly positive shape and rate hyperparameters $\alpha_x, \alpha_y, \beta_x$, and β_y . The final Bayesian hierarchical model is summarized in Fig. 1. The resulting conditional distribution $\pi(\mathbf{x}|\mathbf{y}, \kappa_{\mathbf{y}}, \kappa_x)$ for the true underlying data \mathbf{x} , is again an IGMRF with precision matrix $\kappa_x \mathbf{Q}$, where the conditional distributions for the unknown parameters of the normal-gamma model can be identified as Gamma distributions.

$$\mathbf{x}|\kappa_x, \kappa_{\mathbf{y}}, \mathbf{y} \sim \mathcal{N}_{\mathcal{C}}(\kappa_{\mathbf{y}} \mathbf{y}, \kappa_x \mathbf{Q} + \kappa_{\mathbf{y}} \mathbf{I}_n), \quad (2)$$

$$\kappa_x|\mathbf{x}, \mathbf{y} \sim \text{Gamma}\left(\alpha_x + \frac{n-2}{2}, \beta_x + \frac{1}{2} \mathbf{x}^\top \mathbf{Q} \mathbf{x}\right), \quad (3)$$

$$\kappa_{\mathbf{y}}|\mathbf{x}, \mathbf{y} \sim \text{Gamma}\left(\alpha_y + \frac{n}{2}, \beta_y + (\mathbf{y} - \mathbf{x})^\top (\mathbf{y} - \mathbf{x})\right).$$

In equation (2), $\mathcal{N}_{\mathcal{C}}$ denotes the canonical parametrization of a multivariate normal distribution. These three distributions can be identified as the full conditional distributions of the Bayesian hierarchical model. As these are of closed form, we can use an efficient Gibbs sampling approach to resample the spatial data (Gerber and Furrer, 2015).

To construct a spatial-weight matrix \mathbf{Q} for spatial data on a lattice, as used in equation (1), (2) and (3), we assume that the underlying spatial process is an IGMRF of first order, that is, dependent on first-order neighbor locations. If a higher-order IGMRF fits the data more closely, these derivations work similarly. An IGMRF of first order is an improper GMRF with precision matrix of rank $n-1$, such that $\sum_j \mathbf{Q}_{ij} = 0$ for all $i \in \{1, \dots, n\}$ (Rue and Held, 2005). If the data are distributed on a regular lattice \mathcal{I}_n with $n = n_1 n_2$ nodes, where (i, j) denotes the i th row and j th column, we can define

$$\mathbf{Q} = \alpha_1 \mathbf{R}_{n_1} \otimes \mathbf{I}_{n_2} + \alpha_2 \mathbf{R}_{n_2} \otimes \mathbf{I}_{n_1}. \quad (4)$$

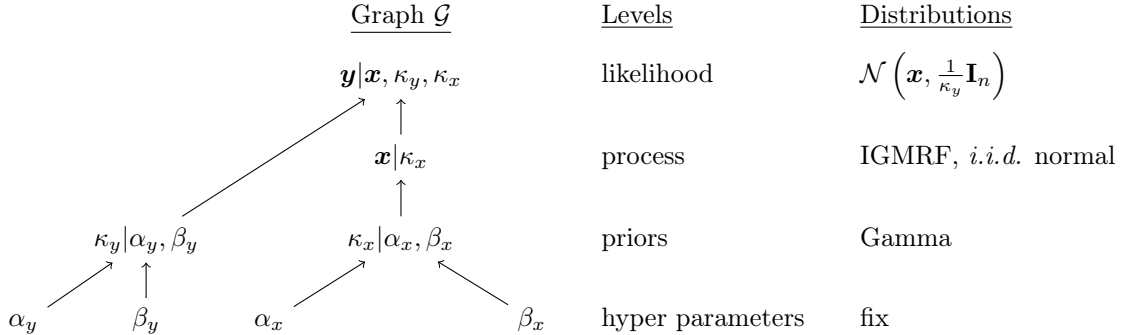


Fig. 1: A graphical-model representation of the Bayesian hierarchical normal-gamma model to resample the observed spatial dataset \mathbf{y} .

\mathbf{R}_n is the structure matrix of a random walk of order one and dimension n :

$$\mathbf{R}_n = \begin{pmatrix} 1 & -1 & & & \\ -1 & 2 & -1 & & \\ & \ddots & \ddots & \ddots & \\ & & -1 & 2 & -1 \\ & & & -1 & 1 \end{pmatrix}$$

The α 's are positive constraints, such that $\alpha_1 + \alpha_2 = 2$, such that possible anisotropic behavior along the two axes can be specified. Assuming that some grid locations do not belong to the area of interest, we need to modify the spatial-weight matrix \mathbf{Q} from equation (4). Knowing the specific locations in the vectorized spatial data \mathbf{x} , we define \mathbf{H} as a diagonal matrix with diagonal entries equal to one if the corresponding (i, j) node of the lattice is to be considered in the analysis, and zero otherwise. The spatial-weight matrix is then calculated as $\mathbf{H}^\top \mathbf{Q} \mathbf{H}$, where \mathbf{Q} is defined in equation (4). Furthermore, the diagonal entries of this matrix $\mathbf{H}^\top \mathbf{Q} \mathbf{H}$ have to be adjusted such that row sums are equal to zero. This approach can be used to ignore vast or small areas as well as to account for irregular boundaries of spatial data. It is a particular case of spatial data distributed on an irregular lattice. For an arbitrary irregular lattice, the spatial-weight matrix can be constructed according to adjacency relations of the associated graph to the IGMRF. An adjacency relation is fulfilled if two nodes from this graph share an edge. Such relations can be represented with a square matrix, where its elements indicate whether pairs of vertices are adjacent or not (Seidel, 1968).

2.2. Sample missing values

In the following subsection, we assume that the spatial input data contain missing values, which implies that the respective locations have no well-defined values allocated. Common approaches to deal with missing values are imputation methods, which use for instance the average value of the respective neighbors of a location to replace a missing value. However, for the final credibility analysis, imputed values are treated as observed values, although we would intuitively attribute more uncertainty and lower credibility to them. To introduce higher uncertainty to locations with missing values, we propose imputing one or multiple values instead, to resample missing values in the spatial data resampling step, as described in Section 2.1. Therefore we assume that the real underlying data \mathbf{x} contain k missing values. Here, we denote \mathbf{H} as the matrix operator from $\mathbb{R}^n \rightarrow \mathbb{R}^m$, such that $m = n - k$, where n is the number of locations on the lattice. The observed dataset $\mathbf{y} \in \mathbb{R}^m$ and $\mathbf{H} \in \mathbb{R}^{m \times n}$ are therefore the identity mapping for the m non-missing values of the observed dataset \mathbf{y} . With the help of \mathbf{H} we can transform the likelihood function of the model to $\mathbf{y}|\mathbf{H}\mathbf{x}, \kappa_y \sim \mathcal{N}\left(\mathbf{H}\mathbf{x}, \frac{1}{\kappa_y}\mathbf{I}_n\right)$. Only the non-missing data affect the posterior samples. The missing values are sampled, based on the values of the neighbors and the prior influence. According to this transformation,

we adjust the hierarchical model in Fig. 1 by replacing \mathbf{x} with $\mathbf{H}\mathbf{x}$. The full conditional distributions, which define the Gibbs sampler, are adjusted to

$$\mathbf{x}|\boldsymbol{\kappa}, \mathbf{y} \sim \mathcal{N}_{\mathcal{C}} \left(\kappa_y (\mathbf{y}^\top \mathbf{H})^\top, \kappa_x \mathbf{Q}_x + \kappa_y \mathbf{H}^\top \mathbf{H} \right), \quad (5)$$

$$\kappa_x|\mathbf{x}, \mathbf{y} \sim \text{Gamma} \left(\alpha_x + \frac{m-2}{2}, \beta_x + \frac{1}{2} \mathbf{x}^\top \mathbf{Q}_x \mathbf{x} \right), \quad (6)$$

$$\kappa_y|\mathbf{x}, \mathbf{y} \sim \text{Gamma} \left(\alpha_y + \frac{m}{2}, \beta_y + \frac{1}{2} (\mathbf{y} - \mathbf{H}\mathbf{x})^\top (\mathbf{y} - \mathbf{H}\mathbf{x}) \right). \quad (7)$$

2.3. Scale-dependent features

In order to find a decomposition of spatial data to recognize their dominant scale-dependent features, the data are smoothed on multiple scales, and the differences between consecutive smooths are calculated. Let \mathbf{S}_λ be a smoother defined by $\mathbf{S}_\lambda = (\mathbf{I} + \lambda \mathbf{Q})^{-1}$, where λ is the smoothing scale, \mathbf{I} the identity matrix and \mathbf{Q} the spatial-weight matrix for the respective spatial data (according to equation (4)). We interpret the spatial data \mathbf{x} with n locations as a vector in \mathbb{R}^n and smooth it with $\mathbf{S}_\lambda \mathbf{x}$. Considering a sequence of smoothing scales, $0 = \lambda_1 < \lambda_2 < \dots < \lambda_L = \infty$, such that $\mathbf{S}_{\lambda_1} \mathbf{x} = \mathbf{x}$ defines the identity mapping and $\mathbf{S}_{\lambda_L} \mathbf{x} = \mathbf{S}_\infty \mathbf{x}$ the mean. \mathbf{x} can be represented as differences of consecutive smooths: $\mathbf{x} = \mathbf{S}_{\lambda_1} \mathbf{x} - \mathbf{S}_{\lambda_2} \mathbf{x} + \mathbf{S}_{\lambda_2} \mathbf{x} - \dots - \mathbf{S}_{\lambda_{L-1}} \mathbf{x} + \mathbf{S}_{\lambda_L} \mathbf{x}$. Scale-dependent details are then formalized as $\mathbf{z}_\ell = (\mathbf{S}_{\lambda_\ell} - \mathbf{S}_{\lambda_{\ell+1}}) \mathbf{x}$ for $\ell = 1, \dots, L-1$ and $\mathbf{z}_L = \mathbf{S}_\infty \mathbf{x}$. Exploiting the sparse structure of the spatial-weight matrix \mathbf{Q} , we solve the linear system $(\mathbf{I} + \lambda \mathbf{Q})^{-1} \mathbf{x}$ and decompose the spatial data as

$$\mathbf{x} = \sum_{i=\ell}^{L-1} (\mathbf{S}_{\lambda_i} \mathbf{x} - \mathbf{S}_{\lambda_{i+1}} \mathbf{x}) + \mathbf{S}_{\lambda_\infty} \mathbf{x} = \sum_{\ell=1}^L \mathbf{z}_\ell. \quad (8)$$

A meaningful multiresolution decomposition requires a careful selection of smoothing scales. We follow Pasanen et al. (2013), who introduced the concept of the scale derivative, defined by

$$\frac{\partial \mathbf{S}_\lambda}{\partial \log \lambda} = \mathbf{D}_\lambda \mathbf{x}.$$

The logarithmic scale for λ is motivated by the fact that for increasing smoothing levels, the difference between successive values for λ has to become wider to have an effect on the smooth. The solved derivative is

$$\mathbf{D}_\lambda \mathbf{x} = \lim_{\lambda' \rightarrow \lambda} \frac{\mathbf{S}_{\lambda'} \mathbf{x} - \mathbf{S}_\lambda \mathbf{x}}{\log \lambda' - \log \lambda} = \lambda (\mathbf{I} + \lambda \mathbf{Q}_x)^{-1} \mathbf{Q}_x (\mathbf{I} + \lambda \mathbf{Q}_x)^{-1} \mathbf{x}. \quad (9)$$

For efficient computation, this derivative can be reduced to solve two linear systems, with a single Cholesky factorization. Values for $\lambda_2, \dots, \lambda_{L-1}$ can then be chosen as the local minima of a vector norm $\|\mathbf{D}_\lambda \mathbf{x}\|$. We propose using the Euclidean or maximum vector norm for spatial data.

2.4. Feature width-extents

The application of multiresolution decomposition to spatial data recognizes their dominant scale-dependent features. However, it gives us no estimate for the width of the extent of the scale-dependent features. To assess this width-extent, we calculate the empirical variogram and optimize corresponding Matérn variogram function parameters. We estimate these parameters directly from the details, which are the differences between smooths. The smooths work as a low-pass filter to de-noise or as a high-pass filter to fortify the respective detail. Subsequently, we can assess the width-extent of scale-dependent features with the spatial data-driven effective-range parameter. Therefore we assume the scale-dependent features to be a realization of the spatial process $\{Z(\mathbf{s}) : \mathbf{s} \in \mathcal{D} \subseteq \mathbb{R}^2\}$ (Cressie, 1993). We also assume, similar to the IGMRF assumptions, that $Z(\cdot)$ is intrinsically stationary, i.e.,

$$\begin{aligned} \mathbb{E}(Z(\mathbf{s}_1)) &\equiv \mu, \\ \text{Var}(Z(\mathbf{s}_1) - Z(\mathbf{s}_2)) &= 2\gamma(\mathbf{s}_1 - \mathbf{s}_2) \end{aligned}$$

for all locations $\mathbf{s}_1, \mathbf{s}_2 \in \mathcal{D}$. Thereby 2γ denotes the variogram and γ the semi-variogram function. The difference $\mathbf{h} = \|\mathbf{s}_1 - \mathbf{s}_2\|$ expresses the spatial lag between two spatial locations. Often the variogram is parametrized with a nugget effect θ_3 : $\gamma(\mathbf{h}) \rightarrow \theta_3$ as $\mathbf{h} \rightarrow \mathbf{0}$ (if it exists); the partial sill θ_2 : the difference of the maximum value of the semi-variogram and the nugget effect; and the range θ_1 : the distance where the variogram reaches its maximum.

In order to estimate the variogram parameters based on the spatial data, we calculate first the empirical variogram, e.g. (Matheron, 1962),

$$2\hat{\gamma}(\mathbf{h}) = \frac{1}{N_J} \sum_{(i,j) \in J} (Z(\mathbf{s}_i) - Z(\mathbf{s}_j))^2,$$

where $J = J(\mathbf{h}) = \{(i, j) : \mathbf{s}_i - \mathbf{s}_j \in T(\mathbf{h})\}$, $N_J = \text{card}\{J\}$ and $T(\mathbf{h})$ is a specified tolerance region in \mathbb{R}^2 (Cressie, 1993; Deutsch and Journel, 1998). Based on the empirical variogram, we fit a variogram model, optimizing the respective parameters for a Matérn variogram function. A Matérn function is suitable for estimating the parameters of the individual smoothing based components, because of its parameterization with an additional smoothing parameter θ_4 . As we assume stationarity, it holds that the Matérn covariance function $\text{cov}(\mathbf{h}) = -\hat{\gamma}(\mathbf{h}) + \lim_{\|\mathbf{h}\| \rightarrow 0} \hat{\gamma}(\mathbf{h})$ (Cressie and Grondona, 1992). We can calculate the effective-range θ_{eff} , which is defined as the distance where the covariance function attains 5% of the sill (sum of partial sill and nugget) (Banerjee, 2003). For the calculation of the empirical variogram and fitting the variogram function in R we use the packages **fields** (Nychka et al., 2020) and **gstat** (Pebesma, 2004). For non-normal spatial data, the recent work of Oman and Mateu (2019) provides an alternative. In one-dimensional problems, such as time-series, the same approach can be used, but instead of variogram functions, the autocorrelation is estimated.

2.5. Posteriori credibility analysis

We assign credibility to the smoothing scales, the features, and their respective width-extents. Credibility intervals can be constructed for the different smoothing scales by replacing \mathbf{x} in equation (9) and applying it to each posterior sample from the model described in Fig. 1. With such credible intervals, scales can be identified that are credibly different. Thereby, we expect for small smoothing scales wide credibility intervals and for larger smoothing scales narrow intervals. Moreover, as the posterior mean separates the assumed observational noise from the spatial data and is somewhat smoother than the posterior samples, we expect to detect less-credibly different smoothing scales between zero and one on the \log_{10} scale.

To assign probabilities to the details and their respective features, we use probability maps as in the scale space analysis, for example, pointwise (PW) credibility maps, where the ℓ th detail \mathbf{z}_ℓ is considered as a vectorization of an array $\mathbf{z}_{\ell,i}$ and every location $i \in I$, $\mathbf{z}_{\ell,i}$ is divided into three disjoint subsets of I in which the components $\mathbf{z}_{\ell,i}$ jointly differ credibly from zero: $I^b = \{i : \text{P}(\mathbf{z}_{\ell,i} > 0 \mid \mathbf{y}) \geq \alpha\}$, $I^r = \{i : \text{P}(\mathbf{z}_{\ell,i} < 0 \mid \mathbf{y}) \geq \alpha\}$ and $I^g = I \setminus (I^b \cup I^r)$. As PW maps treat every location independently, these can sometimes exhibit only tiny islands of credibility. Contemporary approaches, on the other hand, assign credibility more conservatively to locations but maximize the connectedness of credible locations, as described by Erästö and Holmström (2005).

Similar to constructing credibility intervals for smoothing scales, we can build credibility intervals for the effective-range parameters of the scale-dependent features. Therefore, we consider each calculated detail for each posterior sample of the spatial data and apply the procedure described in Section 2.4. It returns the same number of estimated effective-range parameters corresponding to the number of posterior samples, enabling us to construct a credibility interval.

2.6. Computational and implementation aspects

For the efficient implementation of this spatial multiresolution method, we rely on the sparse structure of the precision and respective spatial-weight matrices for spatial processes. In particular, we use the compressed sparse row format of a matrix (Tewarson, 1973; Buluç et al., 2009). To store a matrix in $\mathbb{R}^{n \times n}$ with w non-zero elements we need therefore w reals and $w + n + 2$ integers compared to $n \times n$ reals. The main

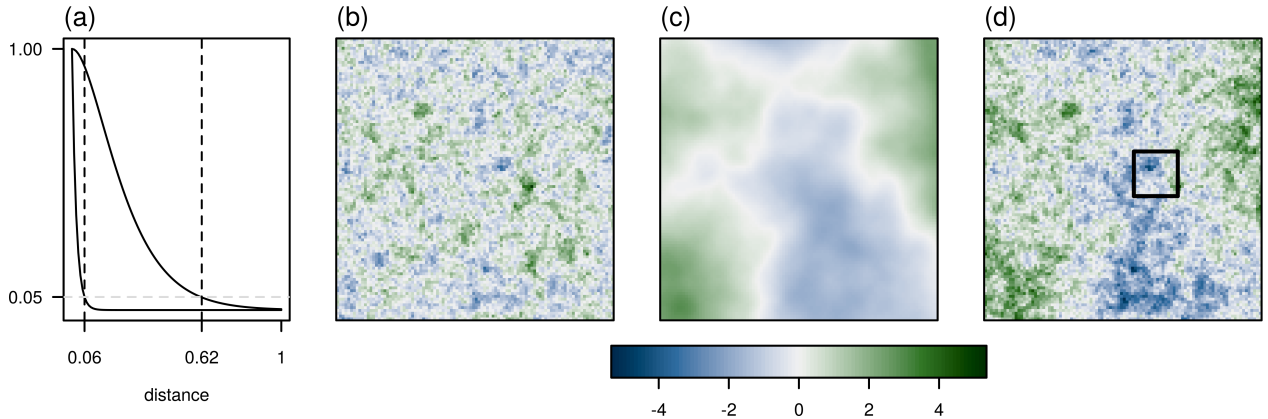


Fig. 2: Visualization of the simulation setup. **(a)** Matérn covariance functions used to simulate the data in **(b)** and **(c)**, where the distance is with respect to the unit interval; **(b)** simulated spatial fields based on a Matérn covariance function with $\theta_{\text{eff}} = 0.06$; **(c)** simulated spatial fields based on a Matérn covariance function with $\theta_{\text{eff}} = 0.62$; **(d)** the sum of the simulated fields **(b)** and **(c)** and additional white noise; the area in the black rectangle is removed, and the respective grid locations are treated as missing values.

computational challenge in the outlined method is the calculation of the inverse of the spatial-weight matrix \mathbf{Q} . We assume \mathbf{Q} is a symmetric positive-definite matrix featuring the aforementioned sparse structure. Instead of intuitively solving $\mathbf{Q}\mathbf{x} = \mathbf{b}$, we proceed by factorizing \mathbf{Q} into $\mathbf{U}^\top\mathbf{U}$, such that \mathbf{U} is an upper triangular matrix, known as the Cholesky factor of \mathbf{Q} . The linear systems $\mathbf{U}^\top\mathbf{y} = \mathbf{b}$ and $\mathbf{U}\mathbf{x} = \mathbf{y}$ are then solved by forward- and backward-solve respectively. To reduce so-called fill-in of the Cholesky factor \mathbf{U} , we permute the columns and rows of \mathbf{Q} according to a permutation \mathbf{P} , i.e., $\mathbf{T}^\top\mathbf{T} = \mathbf{P}^\top\mathbf{Q}\mathbf{P}$, where \mathbf{T} is an upper triangular matrix. More details on the numerical methods for sparse matrices are described in Liu and George (1981); Duff et al. (1986); Dongarra et al. (1998) and Furrer and Sain (2010).

3. Illustration

We illustrate the outlined method with simulated data on a regular grid of size 100×100 over $[0, 1] \times [0, 1]$. We sample two spatial fields based on Matérn covariance functions with different parametrizations, i.e., with range 2 and 12, partial sill 1 each, nugget 0 each, and smoothness 0.5 and 1.8, respectively. The corresponding covariance functions have an effective-range of 0.06 and 0.68, respectively (Fig. 2 (a)). Imitating additive spatial data, we add together these two simulated components and additional white noise to one spatial field (Fig. 2 (b)-(d)). The additional white noise represents observational noise, to simulate observed spatial data as closely as possible. We introduce missing values by removing an area of 15×15 grid points near the center of the simulated data. To assess the sampling quality of these missing values, we apply each step of the identification method to the data with missing values and the data without missing values. For a unique distinction between the analysis of the data with and without missing values, we denote in the following parameters, variables, and details for the data without missing values with an additional prime.

Assuming that we observed the simulated spatial dataset \mathbf{y} or \mathbf{y}' , we iteratively resample it. Thereby we sample values for all locations with missing values, using the Gibbs sampler (Fig. 1) based on the adjusted full-conditional distributions given in equations (5), (6) and (7). The sampler is configured with the vaguely informative hyperparameters, $\alpha_x = 1$, $\alpha_y = 10$, $\beta_x = 0.1$ and $\beta_y = 1$, and after a burn-in phase of length 10'000, a chain of length 1'000 is considered. Standard tools such as trace and autocorrelation are taken into account to assure the convergence of the sample chain (Brooks and Gelman, 1998). Figure 3 (a) shows the width of the 90% posterior interval, and (b) the posterior mean $E(\mathbf{x}|\mathbf{y})$ of all the samples. The grid-pointwise

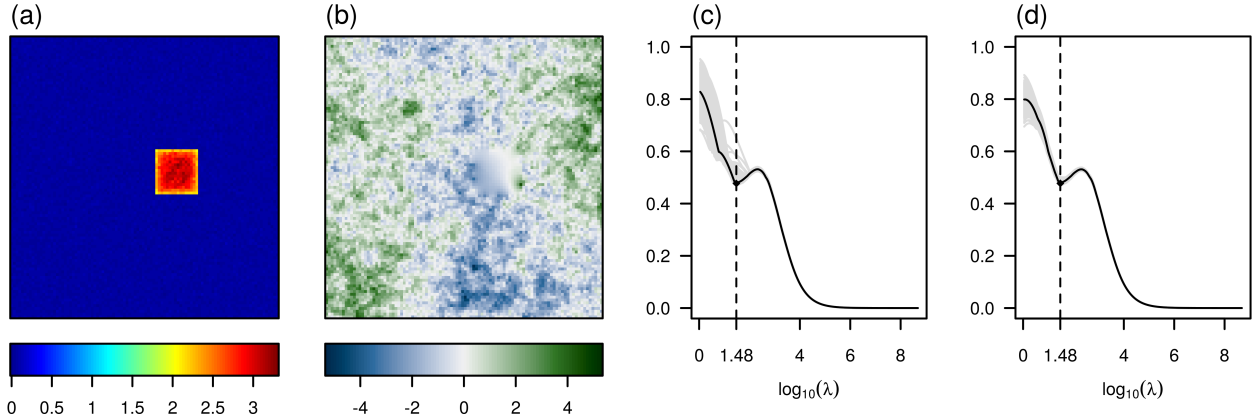


Fig. 3: **(a)** The width of 90% posterior credibility interval for the simulated data with missing values; **(b)** posterior mean of the simulated data with missing values; **(c)**-**(d)** the scale-derivative of the posterior mean of \mathbf{x} (black) and the respective scale derivatives of the individual posterior samples (gray) for based on the simulated data with missing values (c), and for the full dataset (d).

posterior mean smoothes the posterior samples marginally. We exploit this smoothing by assuming that it accounts for observational noise in the spatial data. We can observe this by comparing the simulated field in Fig. 2 (d) with the posterior mean in Fig. 3 (b). For the locations with missing values, the width of the 90% posterior credibility interval is substantially wider for the locations with missing values (Fig. 3 (a)), as additional uncertainty is introduced by sampling the missing values.

We calculate for a sequence of lambdas the scale derivative using the posterior mean for \mathbf{x} in equation (9). We minimize the scale derivative for the maximums vector norm, which is most sensitive for this simulated spatial data. These scale derivatives, as well as the scale derivatives based on the individual posterior samples, are visualized in Fig. 3 (c) and for the complete data in panel (d). Through this procedure, we obtain one scale $\lambda_2 = 30$ with 95% credibility interval (4, 45) and analogously for the simulated data without missing values $\lambda'_2 = 30$ with (3, 40). These smoothing scales have close equivalents, where the credibility interval for the complete data is narrower as there is less uncertainty in the spatial data. For both cases, with and without missing values, $\lambda_1 = 0$ and $\lambda_3 = \lambda_\infty = \infty$ complete the set of smoothing scales.

Based on these derived smoothing scales, we decompose the posterior samples of the simulated spatial data into two details according to equation (8) with $\mathbf{z}_1 = \mathbf{S}_{\lambda_1} \mathbf{x} - \mathbf{S}_{\lambda_2} \mathbf{x}$ and $\mathbf{z}_2 = \mathbf{S}_{\lambda_2} \mathbf{x} - \mathbf{S}_{\lambda_3} \mathbf{x}$ (the overall mean $\mathbf{z}_3 = \mathbf{S}_{\lambda_\infty} \mathbf{x} = 0.03$ completes the decomposition). The resulting details and PW maps are shown in panels (a)-(d) of Fig. 4 when controlling for sampling missing values; the respective details based on the data without missing values are shown in panels (e)-(h). We can recognize dominant features in the two simulated spatial fields in the posterior means of the first and second detail and can assess a good separation into the two components. A comparison of the detail decomposition without missing values with the one with missing values (Fig. 4) shows that this separation is similar for both cases. Moreover, for the second detail, the features in the locations with missing values are partially reconstructed, and the credibility analysis yields similar PW maps.

Next, we estimate the effective-range of the dominant features in the derived details $E[\mathbf{z}_1|\mathbf{y}]$ and $E[\mathbf{z}_2|\mathbf{y}]$, summarized by their posterior mean. We calculate the empirical variogram, fit a Matérn variogram function to estimate its parameter, and calculate the effective-range of the corresponding covariance function. For the respective summarized details $E[\mathbf{z}_1|\mathbf{y}]$ and $E[\mathbf{z}_2|\mathbf{y}]$, the variogram function fits are presented in Fig. 5 (a) and (b). We can construct credibility intervals for the range, partial sill and smoothness parameter of both details \mathbf{z}_1 and \mathbf{z}_2 based on the data with missing values as well as for the details \mathbf{z}'_1 and \mathbf{z}'_2 based on the complete data (Table 1). In each detail, we estimate no nugget effect, and the partial sill therefore

corresponds to the sill parameter. Furthermore, we set for the smoothness parameter an upper bound of value 5, as suggested in the `gstat` package. The smoothness parameter is best estimated based on the shortest distances. However, these are relatively wide on a regular equispaced grid. The numerical conditions to estimate the smoothness parameter are therefore not optimal. Nevertheless, including the estimate of this smoothness parameter increases the quality of the resulting effective-ranges. In general, all the presented estimates are credibly different for detail z_1 and z_2 . The respective credible intervals based on the spatial data with missing values are, in all cases, wider than for the complete data. This also propagates into the resulting effective-ranges. These effective-ranges are close to the ones on which the simulated fields originate. Consequently, we can assess a high quality for the separation of the observed data. With the sampling of the missing values, it is possible to obtain close results, but with more uncertainty. The decomposition by differences of smooths proves useful as a filter of large-scale and small-scale effects. It is possible to recognize the dominant scale-dependent features and assess its respective width-extents, meaning that the dominant features are identified.

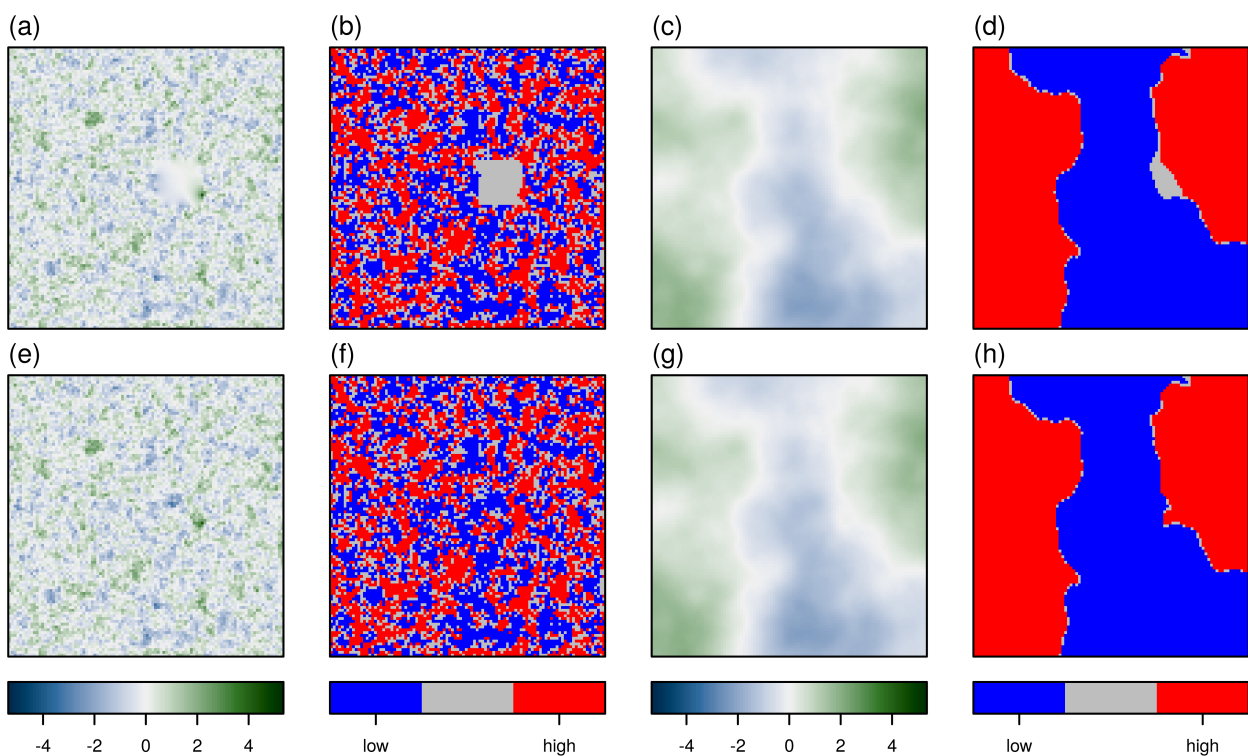


Fig. 4: Multiresolution details for spatial data without missing values. (a) $E[z_1|y]$ summarized by the posterior mean; (b) PW maps of z_1 ; (c) $E[z_2|y]$ summarized by the posterior mean; (d) PW maps of z_2 ; (e)-(h) are the analogous visualizations to (a)-(d) for the spatial data without missing values. Each legend applies for both panels in the same column.

Table 1: Optimized Matérn variogram function parameters and resulting effective-range for the different details summarized by their posterior means and the respective 95% credibility intervals.

detail	range		(partial) sill		smoothness		effective-range		true
	$\hat{\theta}_1$	95% CI	$\hat{\theta}_2$	95% CI	$\hat{\theta}_4$	95% CI	$\hat{\theta}_{\text{eff}}$	95% CI	θ_{eff}
z_1	0.015	(0.014, 0.018)	0.76	(0.79, 0.83)	0.6	(0.5, 0.6)	0.05	(0.05, 0.05)	-
z'_1	0.015	(0.014, 0.018)	0.79	(0.8, 0.84)	0.6	(0.5, 0.6)	0.05	(0.05, 0.05)	0.06
z_2	0.081	(0.079, 0.082)	1.21	(1.19, 1.23)	5	(-, -)	0.66	(0.65, 0.66)	-
z'_2	0.08	(0.08, 0.081)	1.21	(1.2, 1.21)	5	(-, -)	0.65	(0.65, 0.66)	0.62

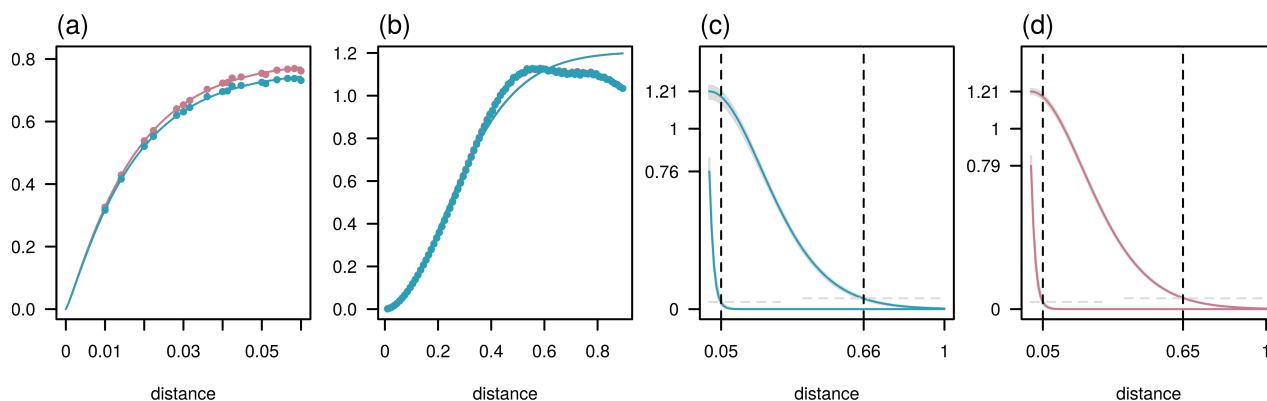


Fig. 5: (a) and (b) the empirical variograms and optimal fitted Matérn variogram functions for the posterior mean of the details z_1 and z_2 ; (c) shows with vertical dashed lines for the details z_1 and z_2 the resulting effective-ranges; (d) shows with vertical dashed lines for the details z'_1 and z'_2 the resulting effective-ranges. Gray dashed horizontal lines indicate 5% of the partial sill. In all panels, the color red indicates values based on the posterior means of the complete spatial data and blue those with missing values. Note, the distances in the individual panels are with respect to the unit interval.

4. Identifying dominant features to find relevant interaction ranges of species

In this section, we describe an application of the outlined feature-identification method to an ecological problem. First, we introduce the observed spatial data and motivate the ecological question for different area sizes in which communities of species interact, and outline the calculation of the biodiversity indices. Second, we describe the preprocessing and the application of the feature-identification method and finally compare the results obtained here to the ones reported in the literature.

4.1. Remote sensing data

A team from the University Zurich, led by the head of the Remote Sensing Laboratories, Prof. Dr. Michael Schaepman, used light detection and ranging (LiDAR) scanning to detect the height, density, and form of trees in forests. They developed precise methods to systematically monitor variability in biodiversity indices based on remote-sensing data (Schneider et al., 2014; Morsdorf et al., 2009). Such data were obtained from the Laegeren mountain site near Zurich, Switzerland. The investigated area is about 2×6 km in extent, and the natural vegetation of the Laegeren mountain is a lightly managed beech-dominated forest, which has a relatively high diversity of tree species, age, and diameter (Eugster et al., 2007). The raw LiDAR measurements were combined to describe specific structural characteristics of the Laegeren mountain forest using morphological traits. For a detailed description and explanation of the selected traits, we refer to Schneider et al. (2014, 2017). The morphological traits we consider are canopy height (CH) of trees in meters (m), plant area index (PAI) in square meter per square meter (m^2/m^2) and foliage height diversity (FHD), a measurement of the amount of foliage at various levels above the ground, converted into an

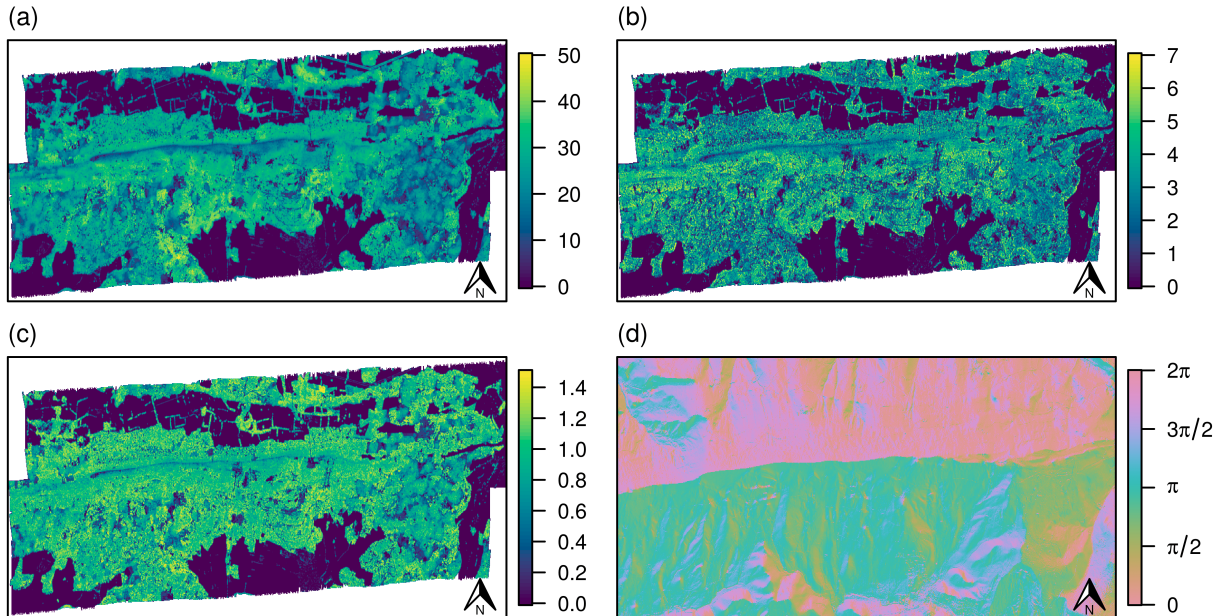


Fig. 6: Morphological traits of the mountain Laegeren. **(a)** Canopy height (CH) in m ; **(b)** plant area index (PAI) in m^2/m^2 ; **(c)** foliage height diversity (FHD) index; **(d)** the topographic variable aspect of the mountain Laegeren in radians.

index. Figure 6 (a)-(c) visualizes these three morphological traits. Apparent features in the traits are the mountain ridge parallel to the x-axis (E–W) and an area of juvenile trees in the south-western part, which is the aftermath of a storm disturbance (Schneider et al., 2017). These traits are calculated per pixel of an overlying equispaced grid, consisting of $400 \times 1'100$ grid points at distances of six meters. With such continuous area-based data, contributions of more than one individual or species to the trait in a single-pixel are possible. Therefore, a pixel does not represent a direct link to an individual specimen. Figure 6 also shows that the traits do not entirely cover the overlying grid of the rectangular area.

4.2. Ecological context

In plant ecology, it is assumed that vegetation is spatially heterogeneous and features emerge as a result of interaction between species. Thereby interaction happens on different scales between different communities of species (Greig-Smith, 1979). In the morphological traits of the mountain Laegeren forest, a community of species could be defined by single trees, by small troops of trees which expanded together or larger assemblages of trees which define ecosystems of different sizes. The interaction range of species within such a community is therefore of particular interest, as these define dominant spatial features and thereby influence measures for its ecosystem functioning and performance (Liu et al., 2018).

Functional biodiversity indices are measures that aim to explain the susceptibility of the forest to climate change or its ecosystem functioning and performance. Various diversity definitions exist, as well as several indices to quantify those. We use the multidimensional functional diversity indices richness, divergence, and evenness (Villéger et al., 2008). These multidimensional functional diversity indices are calculated based on multiple trait data and a moving-window approach (see Appendix B for details). The moving window maps neighboring pixels in a predefined radius, which has the advantage that intraspecific diversity is included and that it is independent of vegetation units, species, or plant functional types (Schneider et al., 2017). When calculating these multidimensional functional diversity indices, the choice of the moving window radii is of paramount importance. To choose suitable radii, Schneider et al. (2017) proposed to calculate the indices for a reasonable range of radii and select the radius for which the overall average index curve has the

steepest gradient. This procedure is typically applied to the entire study area, as well as to some subareas chosen based on expert knowledge. However, dependent on the size and resolution of the data, calculation of the indices takes a considerable amount of time, due to its computational efforts ($\mathcal{O}(n^2 \log(S))$) per radius and different indices (Chazelle, 1993; Pettie and Ramachandran, 2002). From an ecological perspective, it is interesting to understand, on which radii different features for these multidimensional functional diversity indices become manifest.

4.3. Application

Motivated by such ecological questions, we show the feasibility of the feature-identification procedure outlined in Section 2, with the data and diversity indices from above. We apply the multiresolution decomposition to each trait recognizing its dominant scale-dependent features and determine the effective-range of the scale-dependent feature. Assuming that the spatial dependency assesses relevant interaction between species, we interpret the effective-range here as the interaction range, which defines the typical diameter of a community of species. As the interaction range of each component is based on the dominant scale-dependent feature, we further propose that the interaction ranges are suitable candidates for the moving-window radius to calculate the multidimensional functional diversity indices.

From an ecological perspective, it is also interesting to understand which environmental variables affect the variability of the resulting functional diversity. As previous studies of this area have shown, the variance of biodiversity indices based on morphological traits can be partially explained with topographic variables such as altitude, slope, and aspect (Schneider et al., 2017). To take these factors into account, we detrend each morphological trait before the decomposition, according to these variables for the mountain Laegeren. The source for altitude, slope, and aspect (Fig. 6 (d)) of the Laegeren mountain is <https://geodata4edu.ethz.ch> for the year 2018. To ensure the same resolution for these variables as for the morphological traits, we apply ordinary kriging for spatial interpolation (Cressie, 1993). Then, effective-ranges can be derived based on the decomposition of these topographic variables and compared to the interaction ranges based on the trait data. Thereby, it is possible to put into context the derived effective-ranges and subsequent radii and the variables from which these origins.

In the following, we describe the individual steps to derive interaction ranges and moving-window radii for the diversity indices. The standardized residuals of the detrended traits ensure equal weighting in the diversity indices and fulfill the theoretical assumptions of the multiresolution decomposition. Because of the eminent ridge in the forest area, the model depicted in Fig. 1 with an IGMRF precision matrix of order one is well suited to represent the dependencies between locations. The size of the overlying grid of the Laegeren area determines the initial dimension of the precision matrix. As the traits do not entirely cover its overlying grid, we remove the dependencies in the precision matrix for which no observations are available. To reconstruct the traits, we calibrate the model with hyperparameters $\alpha_x = 0.1$, $\beta_x = 0.0005$ and $\alpha_y = 10$, $\beta_y = 1$, such that the prior distributions are vaguely informative. After a burn-in phase of 10'000 draws, we consider 1'000 samples for further analysis.

We calculate the scale derivatives (according to equation (9)) and determine local minima regarding the Euclidean and maximum vector norm for smoothing-scale candidates. This is done for the three traits as well as for the topographic variables and summarized in Table 2. To determine smoothing scales using the scales derivatives, we choose the local minima of the maximum norm (Fig. 7).

Next, we calculate the details of the multiresolution decomposition as differences of consecutive smooths, using the selected smoothing scales, see Figs 8 and 9 for the resulting details. Based on these details, we calculate the empirical variograms and fit a Matérn variogram function to estimate its respective effective-range parameter, in number of pixels. To account for the non-isotropic nature of the respective features, we use directional variograms in east–west (E–W) and north–south (N–S) direction. These empirical variograms and their parameters are estimated for the details based on the posterior mean as well as for the individual posterior samples, to calculate credibility intervals for the estimates. As we estimate the variogram parameters for each trait, each detail, and each posterior sample, we use subsampling for computational competitiveness. To select a subsample, we can exploit the E–W and N–S directions of the dominant features given by the specific topology of the mountain Laegeren area. We estimate variogram functions in E–W direction based on a subsample of whole E–W-transects and analogous for the N–S directional variograms. To reliably and

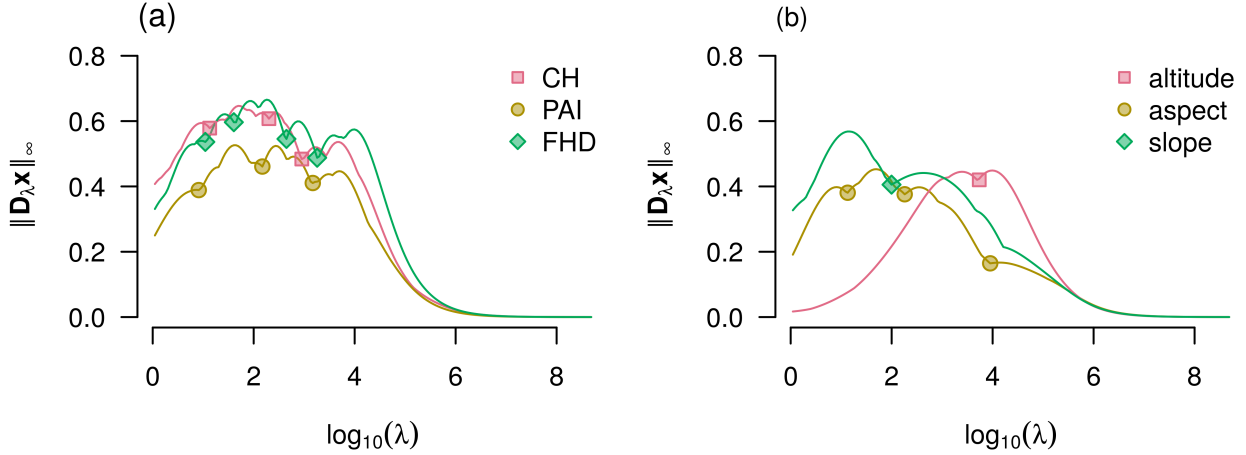


Fig. 7: Scale derivatives for different lambdas, squares, circles, and triangles show the minima of the maximum norm for the individual datasets. (a) scale derivatives for the morphological traits; (b) scale derivatives for the topographic variables of the mountain Laegeren.

Table 2: Minima by scale derivative for Euclidean and maximum vector norms.

norm \ dataset	CH	PAI	FHD	altitude	aspect	slope
$\ \mathbf{D}_\lambda \mathbf{x}\ _2$	28	27	23	4800	12	1, 4800
$\ \mathbf{D}_\lambda \mathbf{x}\ _\infty$	13, 200, 897	8, 148, 1480	11, 40, 445, 1808	4917	13, 181, 8955	99

efficiently estimate the directional variogram function parameters, it is sufficient, to randomly select one of every three consecutive transects. This transect subsampling enables us to calculate the credibility intervals for each estimated effective-range parameter for a scale-dependent feature and select the credibly different radius among all variables.

4.4. Results

A summary of the effective-range, based on the estimated range, partial sill and smoothness parameter of a Matérn covariance function (Section 2) and the respective 95%-credibility intervals of the directional variogram functions is given in Table 3. The morphological-trait details are each more distinctive in E–W direction than in N–S except for the most extensive details, including global trends of the area. This is in contrast to the topographic variables, for which no clear pattern appears. CH and PAI are decomposed in four details, for the first two and the fourth CH has slightly more extensive effective-ranges and PAI for the third one. The trait FHD shows an additional dominant feature compared to the other two traits, where CH- \mathbf{z}_2 and PAI- \mathbf{z}_2 are identified as a pronounced E–W elliptic feature and FHD- \mathbf{z}_2 is rather homogeneous but with smaller width-extent. Moreover, FHD- \mathbf{z}_3 and FHD- \mathbf{z}_4 are similar to \mathbf{z}_2 and \mathbf{z}_3 of CH and PAI, but also broader in extent. Also here, the identified global features are for all three traits similar and most extensive in extent for PAI. Based on these trait details we identify six different width-extents: 7.57 (CH- \mathbf{z}_1), 14.95 (FHD- \mathbf{z}_2), 34.21 (FHD- \mathbf{z}_3), 67.46 (PAI- \mathbf{z}_3), and 130.37 (FHD- \mathbf{z}_4), in number of grid points.

In addition, we can estimate effective-ranges based on the topographic variables; altitude and slope are decomposed in two and aspect in four details. The magnitude of the smoothing scale for the variable altitude implies one detail is describing regional and one global feature. We therefore consider an additional effective-range 270.73 based on the altitude. The variable aspect shows four details were aspect- \mathbf{z}_1 is similar to CH- \mathbf{z}_1 , aspect- \mathbf{z}_2 is similar to FHD- \mathbf{z}_3 , and aspect- \mathbf{z}_3 is between PAI- \mathbf{z}_3 and FHD- \mathbf{z}_4 . These similarities show how the topographic variable aspect partially explains the respective dominant features, which is consistent with the analysis from Schneider et al. (2017). The variable slope is decomposed into two details,

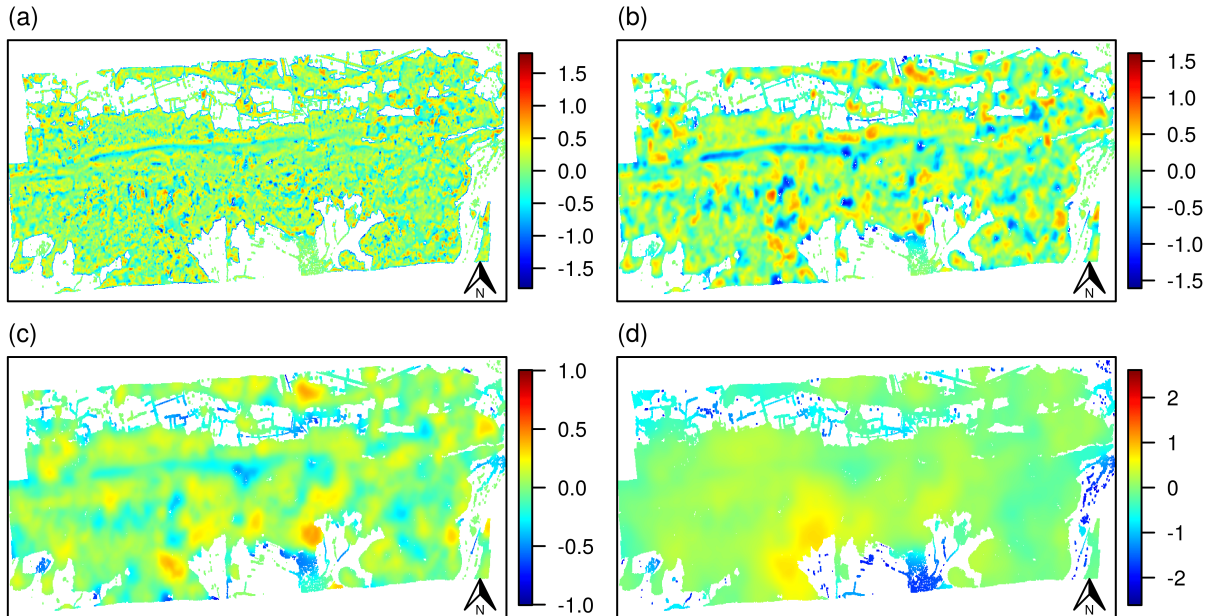


Fig. 8: Scale-dependent details summarized by their posterior means for the morphological trait CH. (a) $E[z_1|\mathbf{y}]$ for $\lambda_1 = 0, \lambda_2 = 13$; (b) $E[z_2|\mathbf{y}]$ for $\lambda_2 = 13, \lambda_3 = 200$; (c) $E[z_3|\mathbf{y}]$ for $\lambda_3 = 200, \lambda_4 = 897$; (d) $E[z_4|\mathbf{y}]$ for $\lambda_4 = 897, \lambda_\infty$.

in a local one, which is similar in width-extent to FHD- z_2 , and a global one; both are more pronounced in E–W direction.

The 95%-credibility intervals are non-overlapping for all range parameters within each spatial dataset. This implies that the respective details contain credibly different dominant features, which we identified. The credibility intervals of these estimates are, as expected, narrow for small effective-ranges and broader for larger effective-ranges.

Finally, we can choose the radii based on half of the estimated feature width-extents, multiplied by the grid-point distance of six meters and rounded to the next natural number. We obtain the set of radii $\{24m, 42m, 102m, 204m, 390m, 810m\}$. Thereof we can exclude the largest one, as its resulting indices would not be reasonable. Comparing the derived radii to the expert-driven set of radii $\{12m, 60m, 240m\}$ from Schneider et al. (2017), it is possible to distinguish a finer set of radii. However, the method missed the smallest interaction range, which is between individual species. This is due to the pixel-based and not species-based data structure and the difficulties of estimating variogram function parameters for small features on regularly gridded data.

The multidimensional indices are finally calculated based on these derived radii shown in Appendix B (Figs B.10, B.11 and B.12). In addition to the determination of moving-window radii, we could find the predominant trait or variable for each radius, which can help to understand the small- or large-scale effect from input data.

5. Discussion

The outlined procedure to identify features in spatial data has several interesting aspects. We show that our spatial multiresolution decomposition is suitable for spatial data. The Bayesian framework of the decomposition permits resampling of missing values, with which it is possible to reconstruct scale-dependent spatial features with according credibility. On the other hand, through the exclusion of areas of no interest, it is possible to precisely model and subsequently decompose the spatial data. A novelty for a multiresolution decomposition is that through the credibility intervals for the scale-dependent feature ranges,

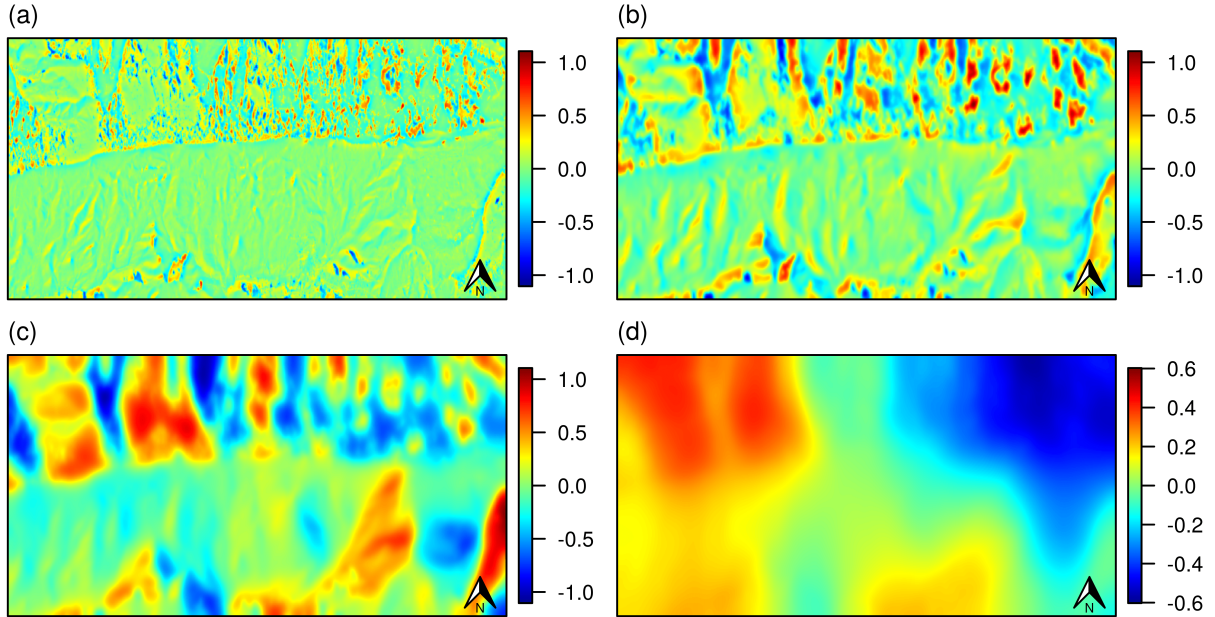


Fig. 9: Scale-dependent details summarized by their posterior means for the topographic variable aspect. (a) $E[\mathbf{z}_1|\mathbf{y}]$ for $\lambda_1 = 0, \lambda_2 = 13$; (b) $E[\mathbf{z}_2|\mathbf{y}]$ for $\lambda_2 = 13, \lambda_3 = 181$; (c) $E[\mathbf{z}_3|\mathbf{y}]$ for $\lambda_3 = 181, \lambda_4 = 8955$; (d) $E[\mathbf{z}_4|\mathbf{y}]$ for $\lambda_4 = 8955, \lambda_\infty$.

it is possible to indicate whether the respective components contain credibly different features. Through the decomposition and the recognition of the scale-dependent features, it is now possible to identify the variogram or covariance parameters of the underlying scale-dependent spatial process. The width-extent assessment for scale-dependent features with effective-ranges is thereby more precise for larger details, based on larger smoothing scales; based on small ones, the smoothing parameter is difficult to estimate on regularly gridded data.

The development of this method and its methodological choices favor structures and techniques that are computationally efficient. Most noteworthy in this context are the sparse structure of the precision matrix, the underlying hierarchical Bayesian model, as well as the transect subsampling scheme for directional variogram functions. Nonetheless, there is more potential computational gain, for example by using so-called tapering functions to estimate the effective-range parameter for scale-dependent features with a maximum-likelihood approach of covariance functions.

The application to scientifically relevant data enables new advances in finding different interaction ranges between species and defining communities of species. Notably, it was possible to respect the strong anisotropic characteristics of the dominant scale-dependent features, given by the topography of the area of interest. A final, careful ecological interpretation or explanation of these different communities would adequately describe the ecosystem functioning and therefore the scale-dependent features in the spatial data.

Acknowledgment

The work was supported by the Swiss National Science Foundation (SNSF 175529, P400P2_186680, P2ZHP2_174828).

Table 3: Estimated effective-range parameters of the respective morphological traits and topographic variables, in number of grid points. The area has 400 grid points in N-S direction and 1'100 grid points in E-W direction.

dataset	detail	direction	$\hat{\theta}_{\text{eff}}$	95% CI
CH	-z ₁	N-S	6.37	(5.90, 6.10)
		E-W	7.57	(7.20, 7.40)
	-z ₂	N-S	19.36	(19.00, 19.20)
		E-W	23.54	(23.10, 23.70)
	-z ₃	N-S	38.64	(38.30, 38.80)
		E-W	59.05	(58.31, 60.51)
	-z ₄	N-S	>400	(>400, >400)
		E-W	390.62	(381.33, 397.74)
PAI	-z ₁	N-S	5.47	(3.80, 4.00)
		E-W	6.16	(4.30, 4.40)
	-z ₂	N-S	16.11	(15.30, 15.60)
		E-W	19.74	(19.10, 19.90)
	-z ₃	N-S	44.10	(42.40, 45.80)
		E-W	67.46	(66.00, 72.51)
	-z ₄	N-S	>400	(>400, >400)
		E-W	382.71	(357.22, 390.87)
FHD	-z ₁	N-S	5.79	(4.70, 4.80)
		E-W	6.50	(5.40, 5.60)
	-z ₂	N-S	13.44	(12.90, 13.10)
		E-W	14.95	(14.30, 14.60)
	-z ₃	N-S	25.01	(24.60, 25.00)
		E-W	34.21	(33.30, 34.60)
	-z ₄	N-S	61.41	(57.51, 65.51)
		E-W	130.37	(118.91, 132.51)
	-z ₅	N-S	>400	(>400, >400)
		E-W	486.30	(382.93, 503.07)
altitude	-z ₁	N-S	153.35	(153.11, 153.41)
		E-W	270.73	(268.42, 272.52)
	-z ₂	N-S	333.63	(338.93, 339.13)
		E-W	489.98	(509.15, 512.55)
aspect	-z ₁	N-S	10.04	(6.20, 6.40)
		E-W	7.99	(5.20, 5.40)
	-z ₂	N-S	26.66	(25.60, 26.00)
		E-W	23.74	(23.00, 23.30)
	-z ₃	N-S	119.15	(116.61, 121.51)
		E-W	82.81	(82.11, 83.71)
	-z ₄	N-S	>400	(>400, >400)
		E-W	>1'100	(>1'100, >1'100)
slope	-z ₁	N-S	11.18	(10.90, 11.10)
		E-W	21.53	(21.20, 21.70)
	-z ₂	N-S	142.63	(204.72, 206.72)
		E-W	388.34	(572.35, 592.66)

Declarations of interest

none

Author statement

Roman Flury: Conceptualization, Methodology, Data Curation, Visualization, Software, Writing - Original Draft preparation. Florian Gerber: Methodology (sampling missing values), Writing - Review & Editing. Bernhard Schmid: Resources (Laegeren mountain data), Writing - Review & Editing on ecological application. Reinhard Furrer: Supervision, Writing - Review & Editing.

References

- Aakala, T., Pasanen, L., Helama, S., Vakkari, V., Drobyshev, I., Seppä, H., Kuuluvainen, T., Stivrins, N., Wallenius, T., Vasander, H., Holmström, L., 2018. Multiscale variation in drought controlled historical forest fire activity in the boreal forests of eastern fennoscandia. *Ecological Monographs* 88, 74–91. doi:10.1002/ecm.1276.
- Banerjee, S., 2003. *Hierarchical Modeling and Analysis for Spatial Data*. Chapman & Hall/CRC Monographs on Statistics & Applied Probability, CRC Press. URL: <https://books.google.ch/books?id=YqpZKTP-Wh0C>.
- Brooks, S.P., Gelman, A., 1998. General methods for monitoring convergence of iterative simulations. *Journal of Computational and Graphical Statistics* 7, 434–455.
- Buluç, A., Fineman, J.T., Frigo, M., Gilbert, J.R., Leiserson, C.E., 2009. Parallel Sparse Matrix-vector and Matrix-transpose-vector Multiplication Using Compressed Sparse Blocks. SPAA '09, ACM, New York, NY, USA. doi:10.1145/1583991.1584053.
- Chaudhuri, P., Marron, J.S., 1999. Sizer for Exploration of Structures in Curves. *Journal of the American Statistical Association* 94, 807–823. doi:10.1080/01621459.1999.10474186.
- Chazelle, B., 1993. An optimal convex hull algorithm in any fixed dimension. *Discrete & Computational Geometry* 10, 377–409. doi:10.1007/BF02573985.
- Cressie, N., Johannesson, G., 2008. Fixed rank kriging for very large spatial data sets. *Journal of the Royal Statistical Society: Series B (Statistical Methodology)* 70, 209–226. doi:10.1111/j.1467-9868.2007.00633.x.
- Cressie, N.A.C., 1993. *Statistics for Spatial Data*. revised ed., Wiley.
- Cressie, N.A.C., Grondona, M.O., 1992. A comparison of variogram estimation with covariogram estimation, in: *The Art of Statistical Science*. Wiley, pp. 191–208.
- Delcourt, H.R., Delcourt, P.A., 1988. Quaternary landscape ecology: Relevant scales in space and time. *Landscape Ecology* 2, 23–44. doi:10.1007/BF00138906.
- Deutsch, C.V., Journel, A.G., 1998. *GSLIB: Geostatistical Software Library and User's Guide*. Second ed., Oxford University Press.
- Dongarra, J.J., Duff, I.S., Sorensen, D.C., van der Vorst, H.A., 1998. *Numerical Linear Algebra for High-performance Computers*. Society for Industrial and Applied Mathematics SIAM.
- Duff, I.S., Erisman, A.M., Reid, J.K., 1986. *Direct Methods for Sparse Matrices*. Oxford University Press, Inc., New York, NY, USA.
- Erästö, P., Holmström, L., 2005. Bayesian multiscale smoothing for making inferences about features in scatterplots. *Journal of Computational and Graphical Statistics* 14, 569–589. URL: <http://www.jstor.org/stable/27594133>.
- Eugster, W., Zeyer, K., Zeeman, M., Michna, P., Zingg, A., Buchmann, N., Emmenegger, L., 2007. Methodical study of nitrous oxide eddy covariance measurements using quantum cascade laser spectrometry over a Swiss forest. *Biogeosciences* 4, 927–939. URL: <https://hal.archives-ouvertes.fr/hal-00297650>.
- Ford, E.D., Renshaw, E., 1984. The interpretation of process from pattern using two-dimensional spectral analysis: Modelling single species patterns in vegetation. *Vegetatio* 56, 113–123. URL: <http://www.jstor.org/stable/20146072>.
- Furrer, R., Sain, S.R., 2010. spam: A sparse matrix R package with emphasis on MCMC methods for Gaussian Markov random fields. *Journal of Statistical Software* 36, 1–25. URL: <http://www.jstatsoft.org/v36/i10/>.
- Gelfand, A.E., 2012. Hierarchical modeling for spatial data problems. *Spatial Statistics* 1, 30 – 39. doi:<https://doi.org/10.1016/j.spasta.2012.02.005>.
- Gerber, F., Furrer, R., 2015. Pitfalls in the implementation of bayesian hierarchical modeling of areal count data: An illustration using bym and leroux models. *Journal of Statistical Software, Code Snippets* 63, 1–32. doi:10.18637/jss.v063.c01.
- Greig-Smith, P., 1979. Pattern in vegetation. *Journal of Ecology* 67, 755–779. doi:10.2307/2259213.
- Holmström, L., 2010. Scale space methods. *Wiley Interdisciplinary Reviews: Computational Statistics* 2, 150–159. doi:10.1002/wics.79.
- Holmström, L., Pasanen, L., Furrer, R., Sain, S.R., 2011. Scale space multiresolution analysis of random signals. *Computational Statistics & Data Analysis* 55, 2840–2855. doi:<http://doi.org/10.1016/j.csda.2011.04.011>.
- Katzfuss, M., 2017. A multi-resolution approximation for massive spatial datasets. *Journal of the American Statistical Association* 112, 201–214. doi:10.1080/01621459.2015.1123632.
- Katzfuss, M., Cressie, N., 2012. Bayesian hierarchical spatio-temporal smoothing for very large datasets. *Environmetrics* 23, 94–107. doi:10.1002/env.1147.
- Kulha, N., Pasanen, L., Holmström, L., De Grandpré, L., Kuuluvainen, T., Aakala, T., 2019. At what scales and why does forest structure vary in naturally dynamic boreal forests? an analysis of forest landscapes on two continents. *Ecosystems* 22, 709–724. doi:10.1007/s10021-018-0297-2.
- Lehmann, A., Höfllich, K., Post, P., Myrberg, K., 2017. Pathways of deep cyclones associated with large volume changes (lvcs) and major baltic inflows (mbis). *Journal of Marine Systems* 167, 11 – 18. doi:<https://doi.org/10.1016/j.jmarsys.2016.10.014>.
- Lindeberg, T., 1994. *Scale-space theory: A basic tool for analysing structures at different scales*.
- Liu, J., George, A., 1981. *Computer solution of large sparse positive definite systems*. Prentice-Hall, Inc. Englewood Cliffs. NJ 7632, 1981.
- Liu, X., Trogisch, S., He, J.S., Niklaus, P.A., Bruelheide, H., Tang, Z., Erfmeier, A., Scherer-Lorenzen, M., Pietsch, K.A., Yang, B., Kühn, P., Scholten, T., Huang, Y., Wang, C., Staab, M., Leppert, K.N., Wirth, C., Schmid, B., Ma, K., 2018. Tree species richness increases ecosystem carbon storage in subtropical forests. *Proceedings of the Royal Society B: Biological Sciences* 285, 20181240. doi:10.1098/rspb.2018.1240.

- Matheron, G., 1962. *Traité de Géostatistique Appliquée*. Mémoires du Bureau de Recherches Géologique et Minières 14, Editions Technip, Paris.
- Morsdorf, F., Nichol, C., Malthus, T., Woodhouse, I.H., 2009. Assessing forest structural and physiological information content of multi-spectral lidar waveforms by radiative transfer modelling. *Remote Sensing of Environment* 113, 2152 – 2163. doi:<http://dx.doi.org/10.1016/j.rse.2009.05.019>.
- Nychka, D., Bandyopadhyay, S., Hammerling, D., Lindgren, F., Sain, S., 2015. A multiresolution gaussian process model for the analysis of large spatial datasets. *Journal of Computational and Graphical Statistics* 24, 579–599. doi:10.1080/10618600.2014.914946.
- Nychka, D., Furrer, R., Paige, J., Sain, S., Gerber, F., Iverson, M., 2020. *fields: Tools for spatial data*. URL: <https://github.com/NCAR/Fields>, doi:10.5065/D6W957CT. R package version 10.3.
- Oman, S.D., Mateu, J., 2019. The latent scale covariogram: A tool for exploring the spatial dependence structure of nonnormal responses. *Journal of Computational and Graphical Statistics* 28, 127–141. doi:10.1080/10618600.2018.1482766.
- Pasanen, L., Aakala, T., Holmström, L., 2018. A scale space approach for estimating the characteristic feature sizes in hierarchical signals. *Stat* 7, e195. doi:10.1002/sta4.195. e195 sta4.195.
- Pasanen, L., Launonen, I., Holmström, L., 2013. A scale space multiresolution method for extraction of time series features. *Stat* 2, 273–291. doi:10.1002/sta4.35.
- Pebesma, E.J., 2004. Multivariable geostatistics in S: the gstat package. *Computers & Geosciences* 30, 683–691.
- Pettie, S., Ramachandran, V., 2002. An optimal minimum spanning tree algorithm. *J. ACM* 49, 16–34. doi:10.1145/505241.505243.
- Reuter, M., Biasotti, S., Giorgi, D., Patanè, G., Spagnuolo, M., 2009. Discrete Laplace-Beltrami operators for shape analysis and segmentation. *Computers & Graphics* 33, 381 – 390. doi:<https://doi.org/10.1016/j.cag.2009.03.005>. IEEE International Conference on Shape Modelling and Applications 2009.
- Rue, H., Held, L., 2005. *Gaussian Markov Random Fields: Theory and Applications*. Chapman & Hall/CRC, London.
- Schneider, F.D., Leiterer, R., Morsdorf, F., Gastellu-Etchegorry, J.P., Lauret, N., Pfeifer, N., Schaepman, M.E., 2014. Simulating imaging spectrometer data: 3d forest modeling based on lidar and in situ data. *Remote Sensing of Environment* 152, 235 – 250. doi:<http://dx.doi.org/10.1016/j.rse.2014.06.015>.
- Schneider, F.D., Morsdorf, F., Schmid, B., Petchey, O.L., Hueni, A., Schimel, D.S., Schaepman, M.E., 2017. Mapping functional diversity from remotely sensed morphological and physiological forest traits. *Nature Communications* 8, 1441. doi:<https://doi.org/10.1038/s41467-017-01530-3>.
- Seidel, J., 1968. Strongly regular graphs with $(-1, 1, 0)$ adjacency matrix having eigenvalue 3. *Linear Algebra and its Applications* 1, 281 – 298. doi:[https://doi.org/10.1016/0024-3795\(68\)90008-6](https://doi.org/10.1016/0024-3795(68)90008-6).
- Skøien, J.O., Blöschl, G., Western, A.W., 2003. Characteristic space scales and timescales in hydrology. *Water Resources Research* 39. doi:10.1029/2002WR001736.
- Stoll, P., Weiner, J., Schmid, B., 1994. Growth variation in a naturally established population of *pinus sylvestris*. *Ecology* 75, 660–670. URL: <http://www.jstor.org/stable/1941724>.
- Strang, G., 1999. The discrete cosine transform. *SIAM Rev.* 41, 135–147. doi:10.1137/S0036144598336745.
- Tewarson, R., 1973. *Sparse Matrices. Mathematics in science and engineering : a series of monographs and textbooks*, Academic Press. URL: <https://books.google.ch/books?id=I-FQAAAAMAAJ>.
- Villéger, S., Mason, N.W.H., Mouillot, D., 2008. New multidimensional functional diversity indices for a multifaceted framework in functional ecology. *Ecology* 89, 2290–2301. doi:10.1890/07-1206.1.
- Wikle, C.K., Berliner, L.M., 2005. Combining information across spatial scales. *Technometrics* 47, 80–91. doi:10.1198/004017004000000572.
- Witkin, A.P., 1983. Scale-space filtering , 1019–1022 URL: <http://dl.acm.org/citation.cfm?id=1623516.1623607>.
- Wu, J., 2013. *Hierarchy theory: An overview*. Springer Netherlands, Netherlands. doi:10.1007/978-94-007-7470-4_24.

Appendix A. Source Files

Supplementary material is available in the git repository at: <https://git.math.uzh.ch/roflur/spatialfeatureidentification>. It contains the following source files.

- README.txt: description of how to install devel packages, to access the data and run the illustration and application of this paper.
- source/: containing sources of devel packages that are used for running the code in analysis/.
- data/: containing R-scripts to load and transform input data
- analysis/: containing R-scripts to run illustration and application.

Appendix B. Multidimensional functional diversity indices

Appendix B.1. Description

Functional richness (FRich) measures the extent of functional space which is occupied by a community of species. It is calculated as the convex hull volume in the space spanned by the multiple traits within the given radius of neighboring pixels Villéger et al. (2008). The definition implies an increase of the indices value with the radius of the window and is expected to follow on average a log curve for increasing radii (Schneider et al., 2017).

Functional divergence (FDiv) shows how species are distributed within the volume of the multidimensional functional trait space occupied by a community of, e.g., trees. To calculate multidimensional functional divergence, let S be the number of pixels in a community, dG_i the Euclidean distance between the i th pixel and the center of gravity and \overline{dG} the mean distance of the S pixels and the center of gravity. Then,

$$\Delta|d| = \frac{1}{S} \sum_{i=1}^S |dG_i - \overline{dG}|,$$
$$\text{FDiv} = \frac{\overline{dG}}{\Delta|d| + \overline{dG}},$$

such that all pixels are equally weighted (no abundances).

Functional evenness (FEve) is calculated based on the minimum spanning tree (MST) of the S pixels within a community. EW_l denotes the (Euclidean) length of the l th branch of the MST, which is used to define the partially weighted evenness

$$\text{PEW}_l = \frac{\text{EW}_l}{\sum_{l=1}^{S-1} \text{EW}_l}$$

and the multidimensional functional evenness

$$\text{FEve} = \frac{\sum_{l=1}^{S-1} \min\left(\text{PEW}_l, \frac{1}{S-1}\right) - \frac{1}{S-1}}{1 - \frac{1}{S-1}}.$$

High functional richness for small window radii shows high diversity within communities and for large window radii high diversity between communities.

Appendix B.2. Results

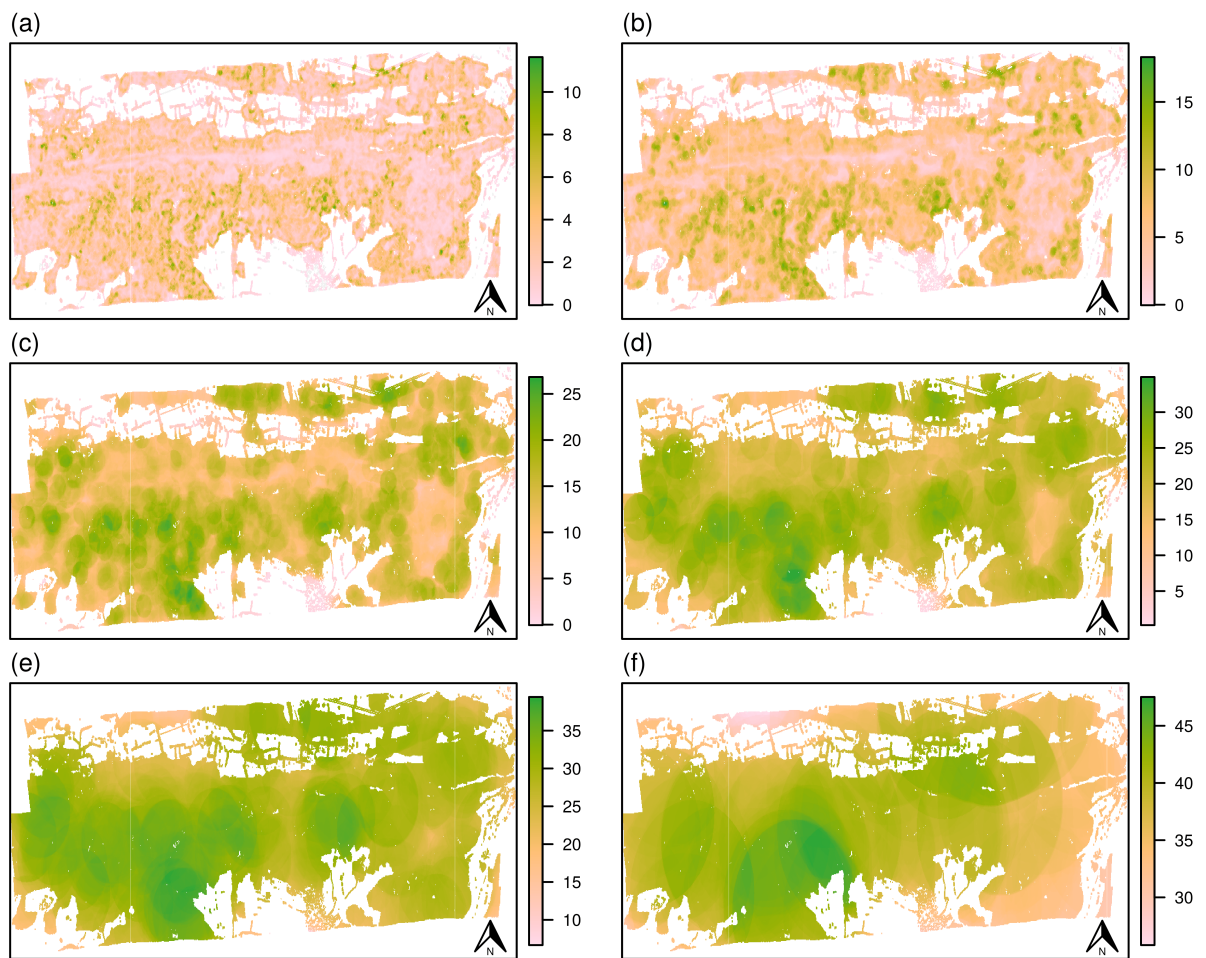


Fig. B.10: Functional richness with moving-window radii $\{24m, 42m, 102m, 204m, 390m, 810m\}$.

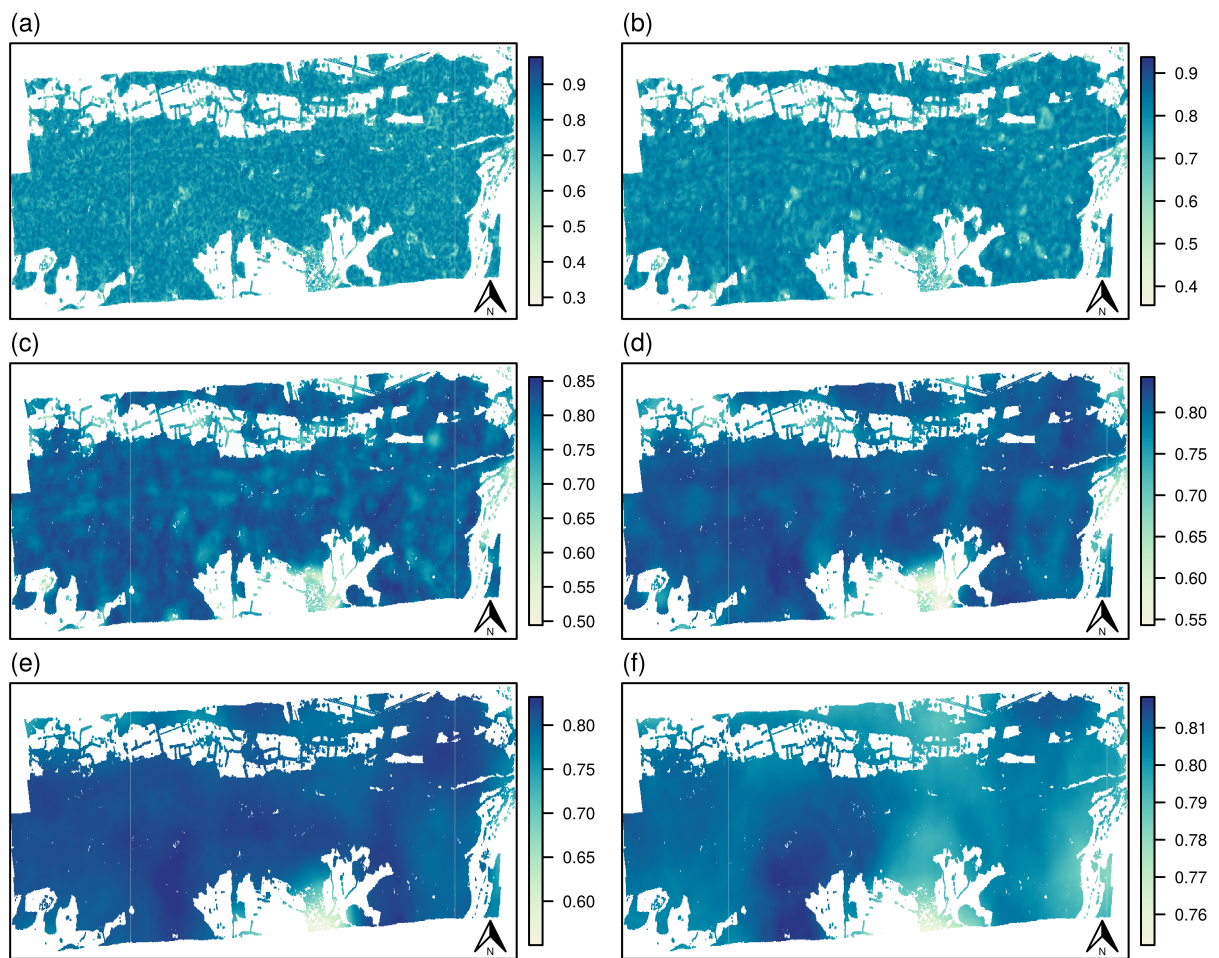


Fig. B.11: Functional evenness with moving-window radii $\{24m, 42m, 102m, 204m, 390m, 810m\}$.

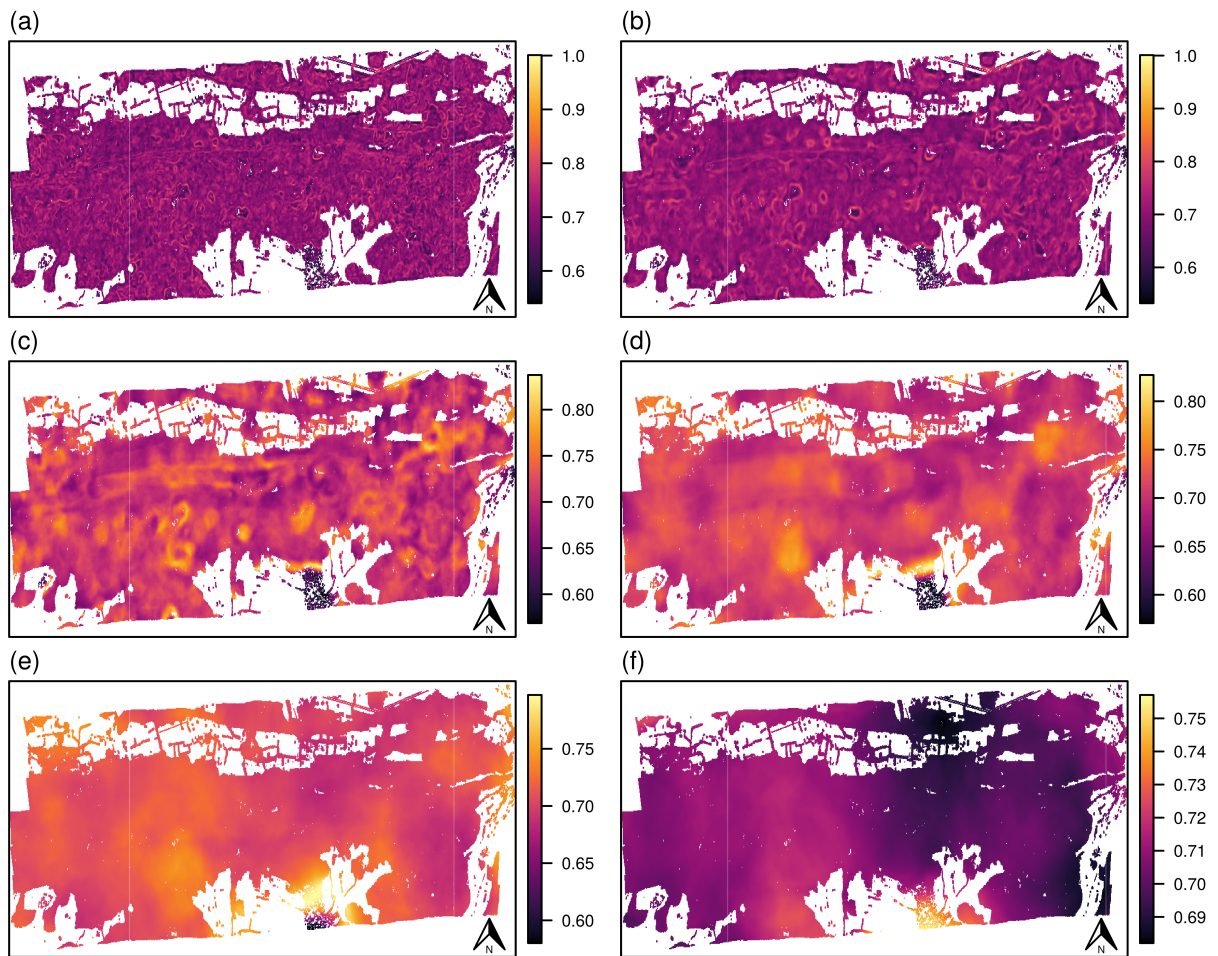


Fig. B.12: Functional divergence with moving-window radii $\{24m, 42m, 102m, 204m, 390m, 810m\}$.